Titania–clay heterostructures with solar photocatalytic applications

C. Belver*, J. Bedia, J.J. Rodriguez

Seccion de Ingenieria Quimica, Facultad de Ciencias, Universidad Autonoma de Madrid, Campus Cantoblanco, E-28049 Madrid, Spain

A B S T R A C T

Several titania–clay photocatalysts were synthesized by a novel route based on a sol–gel approach. The samples were prepared upon exfoliation of a layered clay by the incorporation of the TiO$_2$ precursor. The effect of the clay/TiO$_2$ ratio on the properties and solar photocatalytic activity of the resulting materials was analysed. The catalysts were characterized by X-ray diffraction, UV–vis diffuse reflectance spectra, N$_2$ adsorption–desorption at −196 °C and field emission scanning electron microscopy. The photocatalytic performance was analyzed by the degradation of rhodamine B and phenol in water under solar light. The catalyst with intermediate clay/TiO$_2$ ratio (1/2) showed the highest activity for the photodegradation of both pollutants. In the case of phenol photodegradation, with irradiation times of 24 h fairly high mineralization was achieved with almost complete degradation of phenol and aromatic intermediates and a decrease of the initial ecotoxicity. The synergistic effect of the surface of the clay and the photocatalytic activity of TiO$_2$, controlled by the amount and size of the anatase crystallized, enhances the activity of these titania–clay heterostructures, making them promising materials for solar photocatalytic applications.

© 2015 Elsevier B.V. All rights reserved.

1. Introduction

Photocatalytic technology is one of the advanced oxidation processes (AOPs) that has attracted more attention for water purification. The ability of that technology to remove persistent pollutants and microorganisms from water has been extensively studied and demonstrated [1,2]. It uses a semiconductor able to be excited by photons whose energy is equal to or greater than its band gap giving rise to the generation of electron–hole pairs. The charges created can migrate to the surface and there interact with adsorbed compounds yielding radical species able to induce redox reactions. Continuous research efforts are devoted to improve this technology, mainly related with: (i) the development of highly efficient catalysts under solar light; (ii) the minimization of the electron–hole recombination; and (iii) the removal of the technical barriers that impede its commercialization [1,3]. A diversity of semiconductor photocatalysts have been explored, including metal oxides (i.e., TiO$_2$, ZnO, WO$_3$), mixed oxides, polymetallates (BiVO$_4$, Bi$_2$WO$_6$, SrTiO$_3$), and chalcogenides (i.e., CdS, ZnS, CdSe) [4,5]. Among these photocatalysts, TiO$_2$ has been from long time

the most popular because of its optimum properties, such as high activity, low cost, chemical inertness, photostability, and biocompatibility [6–8]. Nowadays, the TiO$_2$ market is thriving, especially in Asian countries, focusing on the manufacture of photocatalytic coatings and films for self-cleaning and self-sterilizing surfaces. Many technological examples can be found, such as TiO$_2$ coatings deposited on windows and mirrors with antireflection properties, films for air purifiers, or thin films with bactericide applications [9–11].

However, TiO$_2$ has some limitations for photodegradation of organic pollutants in w y due to its poor textural properties and low adsorption capacity. Since there is a direct relationship between the photoefficiency and the active surface of the semiconductor, searching for photocatalysts with appropriate crystal structures and high surface area has a growing interest. In this way, the synthesis of nanostructured catalysts receives special attention. The quantum size effect, due to the reduction of the crystal size, has proved to control the structural and electronic properties yielding photocatalysts with high photoefficiency and improved dispersion capacity [6,12,13]. The separation, recovery and reuse of the titania nanoparticles are critical issues limiting the potential application of photocatalytic technology [1]. Different solutions are currently being investigated to address these technical issues, such as the synthesis of porous photocatalyst structures, the assembling of

nanosized photocatalyst particles on a highly porous solid, the preparation of nanocomposites and the development of films easily removable from aqueous media [1,5,14]. Using porous supports for immobilizing or assembling nanostructured semiconductors may be a useful way to design porous photocatalysts with higher adsorption capacity and active surface than the semiconductors alone, while maintaining structural and electronic properties suitable for application in water treatment under solar irradiation. This includes semiconductor fixation onto several supports, like activated carbon [15,16], clay minerals [17,18] or zeolites [8,19].

Clay minerals have been extensively used as supports in heterogeneous catalysis. Different ways have been developed to create clay-derived heterostructures with photocatalytic applications. Among them, TiO_2-pillared clays (PILCs) have been by far the most studied upon long time. They have been prepared by intercalation of metal-oxopolycations (based on Ti or mixed M/Ti) subjected to a thermal treatment to consolidate pillars of the metal oxide. These materials are characterized by a high surface area and a porous network mainly integrated by micropores [20,21]. Later, new approaches were addressed to create clay-derived heterostructures with modulated and larger porosity than that achieved by common pillaring methods, called porous clay heterostructures (PCHs), although their photocatalytic applications have been so far scarcely reported [22]. A novel approach was recently introduced to develop delaminated porous clay heterostructures (DPCHs) from layered organoclays with a different porous network resulting from delamination and disordering of the clay layers. They represent a novel class of porous materials of high added value. Some works report on the silica and titania–silica assembling over different layered organoclays by a sol–gel route based on the controlled hydrolysis and polycondensation of metal alkoxides yielding porous materials with enhanced textural properties [23]. Following similar approaches other titania–clay materials have been recently prepared from organosepiolite (a fibrous clay) instead of layered clays as support [24,25]. In those cases, the photocatalytic activity under UV light was related to the synergistic effect of the anatase phase and the characteristic textural properties of the sepiolite fibers. In the current work, a novel procedure based on this sol–gel route has been followed for the titanium alkoxide hydrolysis and coagulation in the presence of a commercial organoclay in order to prepare several porous titania–clay heterostructures. This procedure can achieve in a simple way the exfoliation of the clay layers, making accessible their internal surface and allowing the assembling of TiO_2 nanoparticles over them. These materials are interesting candidates for photocatalytic applications and in this work have been tested in the photodegradation of rhodamine B and phenol under solar light irradiation.

2. Experimental

2.1. Materials

A commercial organoclay, named Cloisite® 30B, supplied by Southern Clay Products (Rockwood Company, Texas), has been used. This organoclay is a natural montmorillonite modified with quaternary alkylammonium cations that corresponds to MT_2EtOH (methyl, tallow, bis-2-hydroxyethyl, quaternary ammonium), where the tallow (T) presents the following statistic composition: ~65% C18; ~30% C16; ~5% C14, being chloride the compensating anion. This organoclay has a cation exchange capacity of 0.90 meq/g clay, a basal spacing of 1.78 nm and an organic amount of ca. 30% in weight [26]. Doubly distilled water and 2-propanol (Fluka) were used as solvents. Titanium(IV) isopropoxide (TiIPO, Sigma–Aldrich) was used as titania precursor. Phenol (Sigma–Aldrich, 99%) and rhodamine B (RhB, Sigma–Aldrich, 95%)

have been tested as target pollutants in the photocatalytic activity experiments.

2.2. Preparation of the titania–clay heterostructures

Titania–clay heterostructures were prepared by a heterocoagulation process based on sol–gel technology developed for other oxide–clay heteroestructures [26–29]. The organoclay is dispersed in 2-propanol (10% w/w) under stirring for 24 h to obtain a homogenous suspension. For each titania–clay heterostructure a TiIPO solution (in 2-propanol) was further slowly added to the resulting suspension at 50 °C under continuous stirring, favoring the TiIPO dispersion. The organoclay/TiIPO ratio was adjusted to obtain final clay/TiO_2 weight ratios from 1/0.5 to 1/4 (w/w). After 15 min, a water solution (in 2-propanol as solvent) was slowly added to the suspension, adjusting the amount of water to stoichiometric values just to cause the hydrolysis of TiIPO. Both, TiIPO and water solutions were prepared using 2-propanol as solvent with an alcohol/water molar ratio 1/2. The mixture was maintained under stirring at 50 °C until spontaneous coagulation occurred, giving rise to a dense gel. The time required to complete these gel transitions ranged from minutes to days. The gel was dried overnight at 50 °C and then heated at 550 °C during 4 h in air, just to remove the organic moieties from both the organoclay and the TiIPO. The resulting solids, thus, synthesized were named according to the clay/TiO_2 ratio, hereinafter 1C/0.5Ti, 1C/1Ti, 1C/2Ti and 1C/4Ti.

2.3. Characterization of the solids

X-ray diffraction (XRD) profiles were obtained at room temperature in a Bruker D8 diffractometer with a Sol-X energy dispersive detector, using Cu Kα filtered radiation (λ = 0.15418 nm) in the 2θ range 2–70° with a scanning rate of 1.5° min^{-1}. The structural identification was performed by using the JCPDS cards [30]. Average crystal size (D) was calculated from the most intense diffraction peak (1 0 1) using the Scherrer's equation [31]. Variable temperature XRD (VT–XRD) profiles were performed using an X'Pert Pro Panalytical diffractometer with Ni filtered Cu-Kα radiation and a xenon detector. To perform the high temperature experiments, an anton paar HTK120 heating stage was used, integrated with the Panalytical control software. The as-prepared powders were loaded onto an alumina heater stage. This heater enclosure was purged with air at a flow rate of 2 mL min^{-1}. The sample was further heated at a rate of 10 °C min^{-1} up to a maximum of 800 °C. The sample was held at several target temperatures (each 100 °C) for up to 130 min. During this hold time, the sample temperature was maintained constant and XRD data were collected over the 2θ range 3–70° with a step size of 0.04° and a count time of 4 s.

Textural properties were analysed by N_2 adsorption–desorption at −196 °C using a static volumetric analyser Micromeritics TriStar 123. The specific total surface area was calculated using the Brunauer-Emmett-Teller (BET) method [31,32]. The micropore surface area (S_{MP}), the external or non-microporous surface area (S_{EXT}) and the micropore volume (V_{MP}) were calculated from thet-plot according to De Boer's method [33], while the total pore volume (V_T) of the solids was estimated from the amount of nitrogen adsorbed at a relative pressure of 0.99. The pore size distributions of microporous and mesoporous regions were obtained by the Horvath-Kawazoe [33] and the Barrett–Joyner–Halenda (BJH) [34,35] methods, respectively. UV–vis diffuse reflectance spectra (DR-UV–vis) were recorded on a UV–vis spectrometer (Shimadzu 2501PC) in the 300–900 nm region using the $BaSO_4$ reflectance standard as baseline. Characterization by field emission scanning electron microscopy (FE-SEM) was performed in a FEI microscope NOVA NANOSEM 230 model that allows visualization of samples with various detectors and without the need of being covered with

a conductive coating. Quantitative analyses of the samples were made with the EDX detector (EDAX Genesis XM2i) that allows identification of elements and incorporates software to obtain fast mapping of them.

2.4. Photocatalytic activity experiments

The photocatalytic activity of the samples was evaluated from the degradation of rhodamine B and phenol in aqueous solution. The main objective of this work is to compare the activity of catalysts using the same initial concentration. Because the adsorption capacity of this kind of materials should be different depending on the target compound, we performed a complementary study on rhodamine B and phenol adsorption in dark. This information is included as ESI and the results are depicted in Fig. S3 for the 1C/2Ti catalyst, as representative example. Those results allow knowing the amount adsorbed on each catalyst in dark. Thus, the starting concentration was adjusted in each case so that the initial concentration in all the photocatalytic experiments was $25\,mg\,L^{-1}$ after 2 h of adsorption. The photocatalytic activity experiments were performed with $500\,mg\,L^{-1}$ of catalyst suspended in a 500-mL pyrex glass reactor containing rhodamine B or phenol in a total volume of 300 mL. Air was continuously bubled into the liquid at $50\,mL\,min^{-1}$ flow rate. The experiments were carried out inside a Suntest solar simulator (Suntest XLS +, ATLAS) equipped with a $765–250\,W\,m^{-2}$ Xe lamp ($61–24\,W\,m^{-2}$ from 300 to 400 nm, $1.4 \times 10^{20} – 5.5 \times 10^{19}$ photons $m^{-2}\,s^{-1}$) and a "daylight" filter (cuts off 290 nm), which simulates solar radiation. The reaction temperature was monitored and reached a constant value of $38 \pm 1\,°C$ after the first 20 min of irradiation. The intensity was fixed at $550\,W\,m^{-2}$ for all photocatalytic experiments. The photoreactor included two ports in its top section for sampling the solution and flowing air. Before irradiation, the suspension was stirred in the dark for 2 h to achieve the adsorption equilibrium. Then, the suspension was exposed to light irradiation under magnetic stirring for at least 10 h. At given time intervals, 10 mL of the suspension was collected, and the photocatalyst was removed by filtration using nylon fiber filters (Tecknocroma 0.45 mm). RhB was quantified with a UV–vis spectrophotometer (Cary 60 UV–vis, Agilent Technologies) by integration of the area under the peak at 554 nm characteristic of this compound in the 450–600 nm range. Phenol and other aromatic compounds (hydroquinone, catechol, resorcinol and *p*-benzoquinone) were quantified by means of HPLC (Varian Pro-Start 310) with a diode array detector (330 PDA). Total organic carbon (TOC) was measured using a TOC analyzer (Shimadzu, mod., TOC VSCH). Organic acids (acetic, formic, malonic and oxalic) were measured by ionic chromatography with a Metrohm 790 personal IC. Ecotoxicity measurements were performed by a bioassay following the standard Microtox test procedure (ISO 11348-3, 1998), based on the decrease of light emission by the marine bacteria *Vibrio fischeri* (*Photobacterium phosphoreum*), using a Microtox M500 analyzer (Azur Environmental).

3. Results and discussion

3.1. Synthesis and characterization of titania–clay heterostructures

The synthesis of titania–clay heterostructures is based on a sol–gel technique consisting in controlled hydrolysis and polycondensation of metal alkoxides inside the interlayer region of an organoclay. This procedure has been used for the synthesis of oxide–clay heterostructures with applications in a wide range of possibilities depending on the nature of the oxide and the clay [26,28,29,36]. In this work, a commercial organoclay (Cloisite 30B) has been used as raw material thus avoiding the previous step of synthesizing the organoclay like in other works. That organoclay has a layered structure, typical of smectite clay materials, with an interlayer region occupied by organocations yielding an interlayer distance of 1.78 nm (higher than conventional smectites, ca. to 1.28 nm) and giving to the clay organophilic character. Both aspects favor the further sol–gel transition of TiIPO within the interlayer region of the organoclay. This procedure has been adjusted to achieve the incorporation of TiIPO within layers giving rise to the exfoliation of these layers; thus, losing the preferential order of the clay in the *c* axis and increasing the available surface. The synthetic procedure is schematized in the electronic Supplementary information (Fig. S1, ESI) to provide more details about this method.

Given that the aim of this work is to obtain titania-based photocatalysts, a heating treatment was used to transform the TiIPO precursor into the desired TiO_2 phase. This treatment allows the removal of the organic moieties and the condensation of OH groups in the inorganic network giving rise to the formation of oxide nanoparticles that remain assembled and distributed over the surface of the layers in the final clay nanoarchitectures. The calcina-
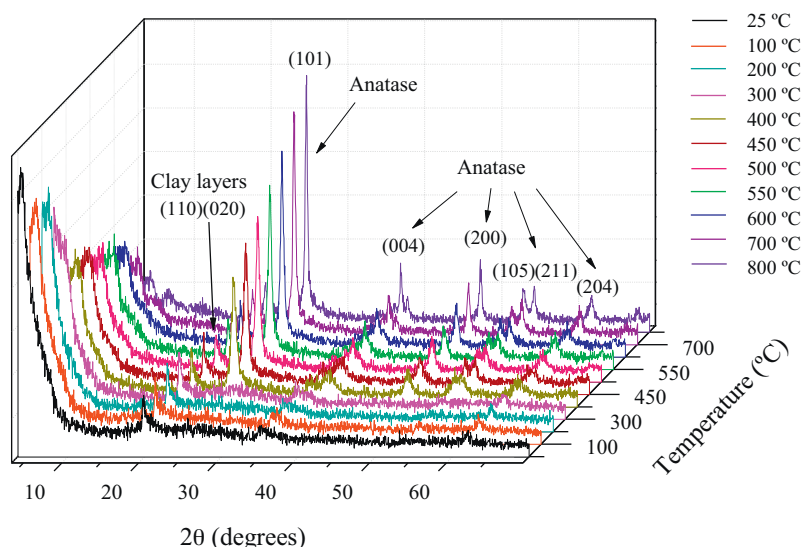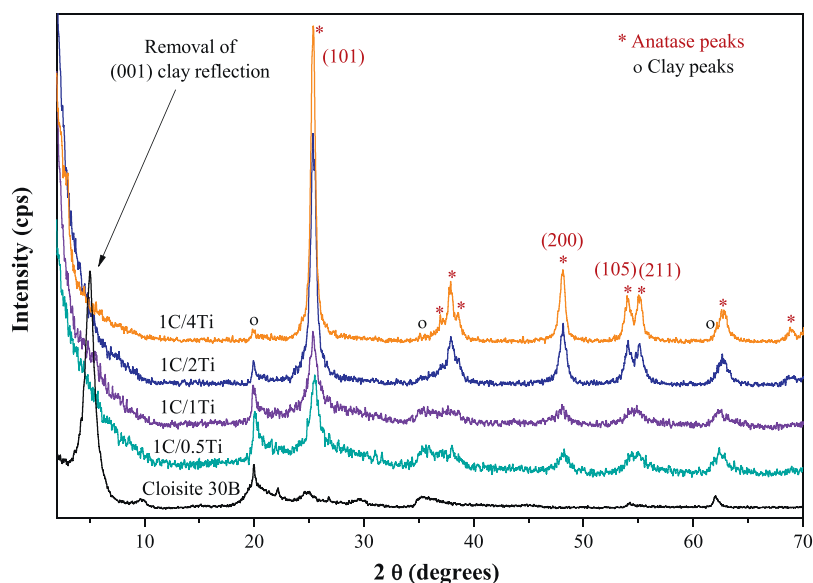

Fig. 1. In situ VT-XRD profiles of 1C/2Ti dried solid before the heating treatment obtained at different temperatures.

Fig. 2. XRD profiles of the pristine organoclay (Cloisite 30B) and the titania–clay heterostructures synthesized. The characteristic peaks of both the anatase and the organoclay are also indicated (in parenthesis are indicated the (hkl) assignation of the most intense peaks of anatase).

tion temperature was selected according to the VT-XRD analyses, recorded in situ from room temperature to 800 °C and made with the 1C/2Ti solid just obtained after the drying process. The diffraction profiles are plotted in Fig. 1. The diffraction peaks of anatase TiO_2 phase (JCPDS card No. 78–2486) begin to make up at 400 °C and the crystallinity increases as the temperature raises. The mean size of anatase crystals was calculated by the Scherrer's equation from the most intense peak (1 0 1). The values obtained at different heating temperatures are collected in Table S1 of ESI. These values increased linearly with temperature from 9.5 nm at 400 °C to 21 nm at 800 °C. Therefore, with this method the anatase phase turns out into the stable TiO_2 phase even at high temperatures maintaining low crystal size values. There are no diffraction peaks due to rutile or brookite phases that tend to appear above ca. 650 °C by other synthesis procedures [12]. Therefore, this simple method allows obtaining anatase nanoparticles with low crystal size over a layered clay. Regarding the organoclay, the diffraction profiles show the typical peaks of smectite clay minerals at 19.9° and 61.8°, although this last overlaps with the (2 0 4) peak of the anatase (at 62.6°). The presence of these peaks shows that the clay layers structure is not destroyed during the synthesis process, even after thermal treatment at high temperatures. Based on these results, a temperature of 550 °C was fixed for treating all the dried solids in order to guarantee the formation of anatase phase with certain degree of crystallinity while low crystal size values.

The titania–clay heterostructures obtained after heating treatment were studied by XRD. The diffraction profiles are displayed in Fig. 2 compared with that of the raw organoclay. As expected, the organoclay suffered a transformation of its layered struc-

ture. The (0 0 1) diffraction peak characteristic of the organoclay, located at 4.9° (2θ), disappeared in the heterostructures. The lack of the (0 0 1) basal reflection indicates that the clay layers stacking become disordered in the c axis, which proves the exfoliation of the clay layers [26–28]. This result confirms also that the TiIPO was able to access to the interlayer clay region during the synthesis, occurring the sol–gel transition inside the interlayer space and giving rise to the desired exfoliation while the titania precursor was incorporated (illustrated in Fig. S1 of ESI). The other (hkl) reflections (Fig. 2) typical of smectite did not suffer modifications during the synthesis. Although the layer stacking was lost, those reflections prove that the layer structure remained unchanged. Thus, the heterostructures maintain the layer structure of the pristine organoclay although without ordering. The XRD profiles of titania–clay heterostructures also show diffraction peaks associated with the crystallization of titania in its anatase phase (JCPDS card No. 78-2486). The anatase formation is evident in all diffractograms although its crystallinity depends on the amount of TiO_2 incorporated. To check the anatase crystallization, the crystal size of anatase was calculated from (1 0 1) reflection by the Scherrer's equation. The results are collected in Table S2 of ESI. The crystal size calculated for the 1C/2Ti sample (13.1 nm) matches the value previously estimated from the VT-XRD analyses for the 1C/2Ti dried sample, whose crystal size at 550 °C was ca. 12.5 nm (Table S1 of ESI). Thus, VT-XRD analysis appears as a useful tool to control the synthesis of this kind of heterostructures. The 1C/0.5Ti sample showed the lowest crystal size, 9.6 nm that increases to 15.4 nm for 1C/4Ti, the sample with the highest amount of titania incorporated to the organoclay. The crystallization of anatase does not only

Table 1
Characterization of the porous structure of the catalysts.

Sample	S_{BET} (m²/g)[a]	S_{EXT} (m²/g)[b]	S_{MP} (m²/g)[b]	V_{MP} (cm³/g)[b]	V_T (cm³/g)[c]	Band gap energy (eV)
Cloisite 30B	58	43	15	0.006	0.135	–
1C/0.5Ti	233	124	109	0.057	0.262	3.12
1C/1Ti	190	110	80	0.042	0.234	3.21
1C/2Ti	143	110	33	0.018	0.210	3.18
1C/4Ti	100	83	17	0.009	0.166	3.19

[a] Specific surface area from BET method.

[b] External surface area, micropore surface area and micropore volume, respectively.

[c] Total pore volume at P/P_0 equal to 0.99.

depend on the heating temperature, as it was demonstrated by VT-XRD analyses, but the amount of TiIPO incorporated also affects to that process.

Fig. 3 shows representative FE-SEM images of the starting organoclay and some titania–clay heterostructures (more images are included in Fig. S2 of ESI). The compact layered microstructure of the organoclay turns into a more spongy morphology where the clay layers are no stacked and covered by spongy TiO_2 nanoparticles. These images confirm the disaggregation of the clay particles, observed by XRD, while titania is incorporated and assembled to the clay layers. Apparently, the titania nanoparticles are homogeneously distributed over the clay layers. However, to confirm that quantitative analyses of Si and Ti were performed by EDX for the 1C/1Ti sample. Fig. 4 depicts the mapping of those elements. Si was selected as reference element for the starting organoclay where it is the main element [26,36]. From those mapping images, it can be appreciated a similar distribution of Ti and Si, being both homogeneously distributed along the region analyzed. Therefore, the methodology used in this work, allows synthesizing by a simple procedure disordered porous materials consisting of TiO_2 nanoparticles homogeneously distributed and assembled onto the surface of clay layers.

The porous structure of these titania–clay materials was characterized from the corresponding nitrogen adsorption–desorption isotherms at $-196\,^\circ$C, plotted in Fig. 5, which includes also that of the starting organoclay. This last shows a type II isotherm of the IUPAC classification, with a H3 hysteresis loop [37]. This type of isotherm has been described for several layered clay materials, characterized by porous aggregates with certain rigidity due to the layer packing as a house-of-cards [38,39]. The isotherms for the titania–clay heterostructures are fairly different to that of the starting organoclay. They display nitrogen adsorption at both low and high relative pressures; thus, can be classified as a combination of types I and II [37]. This kind of isotherms is typical of other clay derived materials, such as PILCs, PCHs and DPCHs [36,40]. Those materials are characterized by the presence of micro-, meso- and macropores, whose development is mainly due to the house-of-cards structure formed by the plate-like particles. The formation of that structure has been demonstrated by statistical model for smectite clay suspensions undergoing a sol–gel transition similar to the one occurring in our synthesis method [39]. The porous structure due to the presence of the clay layers is supported by the fact that increasing the amount of titania incorporated decreases the volume of N_2 adsorbed as a result of the increased blockage of the interlayer and the house-of cards stacking spaces. Table 1 summarizes the values of the textural properties obtained from the isotherms of Fig. 5. Note that the low surface area of the starting organoclay, compared with common layered clays, is due to the presence of organic species between the clay layers that partially block the porous network. The titania–clay heterostructures show BET surface area values between 100 and 230 m^2 g^{-1} depending on the TiO_2 amount incorporated, all of them well above that of the starting organoclay and higher than the reported for other titania and titania–heterostructures [29]. That increase of the surface area is due to: (i) the presence of nanoparticles of anatase phase, since the nanostructure induces an increase of surface area by the corresponding decrease of the primary particles size; and (ii) the exfoliation of clay layers that makes accessible their internal surface. The porosity of the final heterostructure depends on the amount of TiO_2 assembled to the clay. Table 1 shows the micropore surface area that increase from 17 to 100 m^2 g^{-1} as the amount of TiO_2 decreases. Thus, increasing the clay to TiO_2 ratio yields heterostructures with higher surface area, associated to higher micropore contribution. This is consequence of the exfoliated layer structure of the clay that favors the accessibility to the internal surface of the layers while developing a disordered porous net-
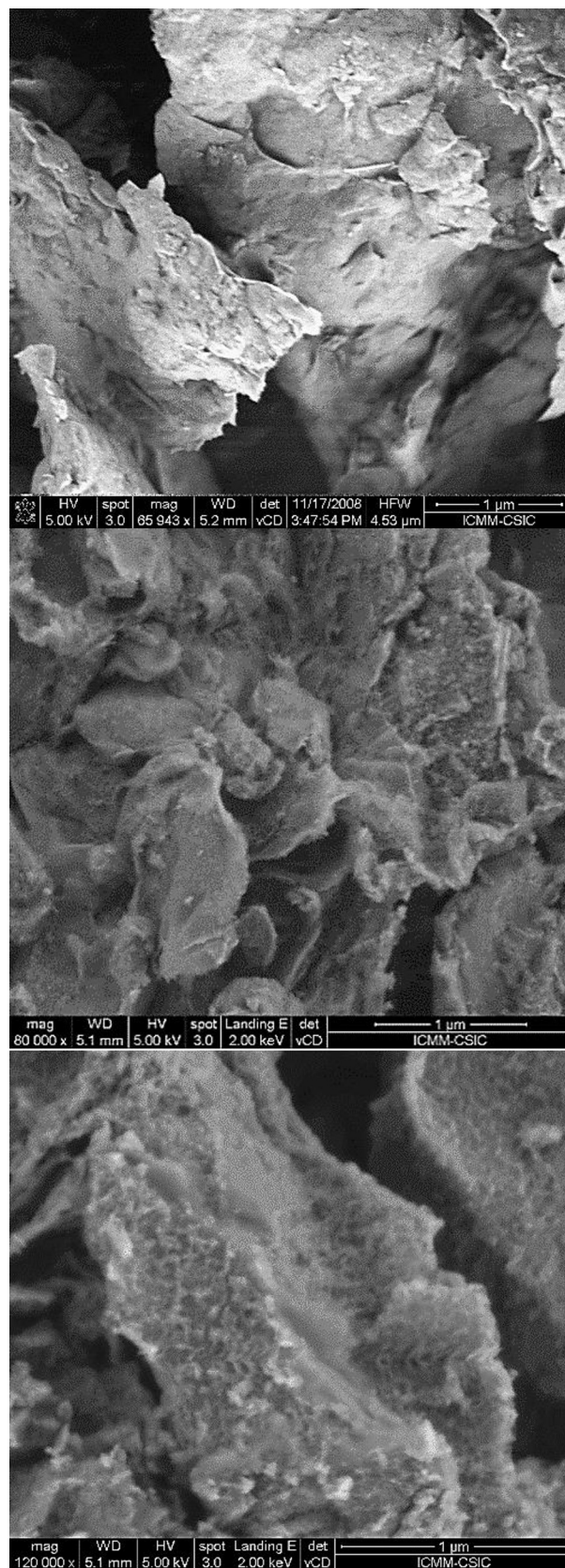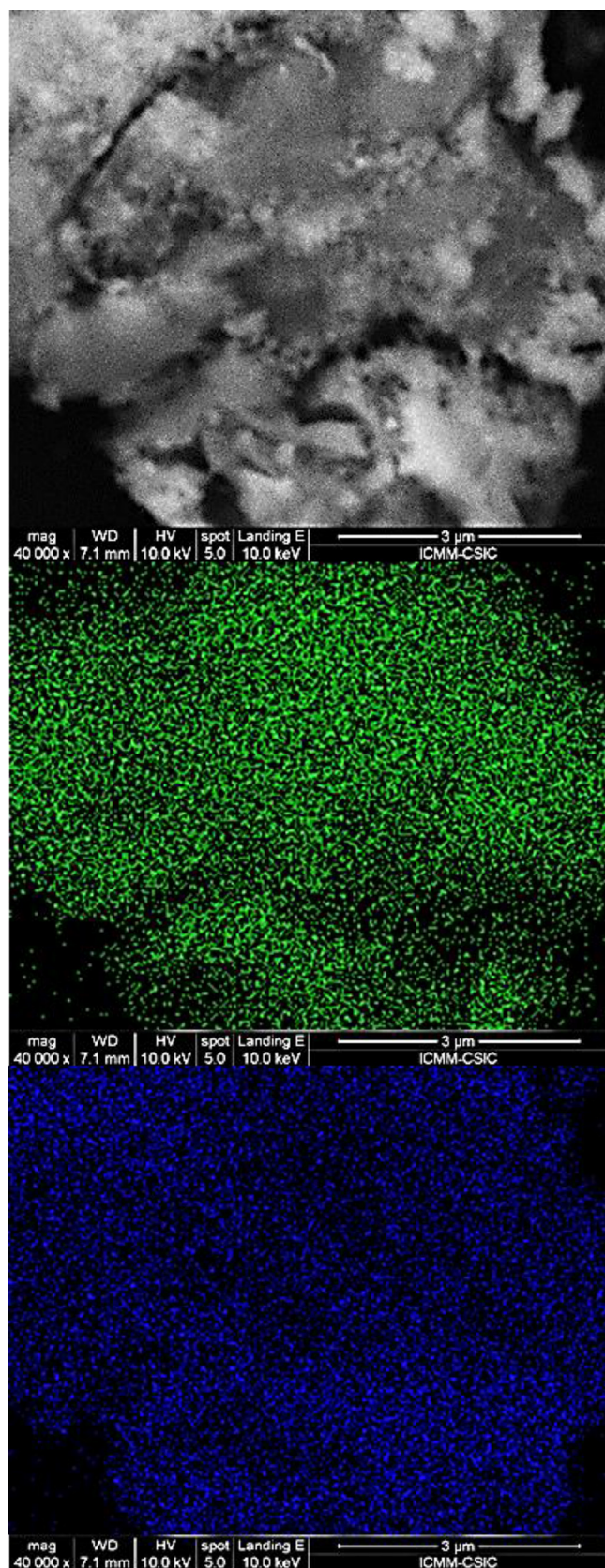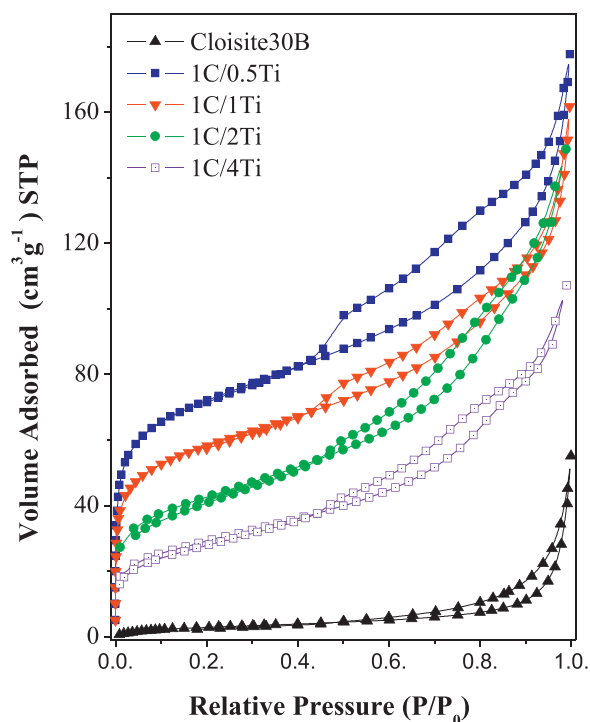

Fig. 3. FE-SEM images of Cloisite 30B, 1C/0.5Ti and 1C/1Ti heterostructures, from left to right.

Fig. 4. FE-SEM image of 1C/1Ti (up) and their corresponding EDX mapping for Si (central) and Ti (bottom) elements.

Fig. 5. N_2 adsorption–desorption isotherms at $-196\,^\circ$C of the titania–clay heterostructures.

work. It should be remarked that according to Fig. 5 and the results of Table 1, these titania–clay heterostructures have a porous network including both, micropores and mesopores with a relative contribution depending on the clay/TiO$_2$ ratio.

To learn more on the evolution of the microporosity and mesoporosity of these heterostructures with the amount of TiO$_2$ incorporated, the micropore and mesopore size distributions were obtained and they are plotted in Fig. 6. All the samples show a fairly wide distribution of micropore size, centered at around 0.8–1 nm, differing from those described for other oxide–clay heterostructures (including PILCs and DPCHs), characterized by a bimodal distribution [26,40]. Increasing the amount of TiO$_2$ incorporated provokes a progressive constriction of the microporosity. Based on the micropore volume values of Table 1 and the evolution of the micropore size distribution, it can be concluded that the anatase phase crystallized in these heterostructures has no microporosity. The porous structure of these materials shows a significant contribution of mesoporosity looking at the values of the external or non-microporous surface area (S_{EXT} in Table 1). Those values represent fairly high percentages of the corresponding BET surface area and are frankly higher than that of the starting organoclay. Thus, the synthesis of the titania–clay heterostructures implies the creation of mesopores as an important issue. Those mesopores are mainly distributed within a narrow range of the lowest size region (see Fig. 6B). The formation of these small mesopores is due to the creation of a mesostructured gallery based on the house-of-cards structure formed by the above mentioned plate-like particles, described also for other layered clay materials. Thus, the method used to synthesize these heterostructured materials allows tuning their porous structure by controlling the clay/TiO$_2$ ratio.

The DR-UV–vis spectra plotted in Fig. 7 provide a picture of the electronic properties of the different samples. As can be seen all the heterostructures show almost equal UV–vis absorption profiles, with an absorption edge located at 390 nm, without significant differences among the samples with different TiO$_2$ amounts. As well described in many studies on TiO$_2$ materials [7,41], the anatase
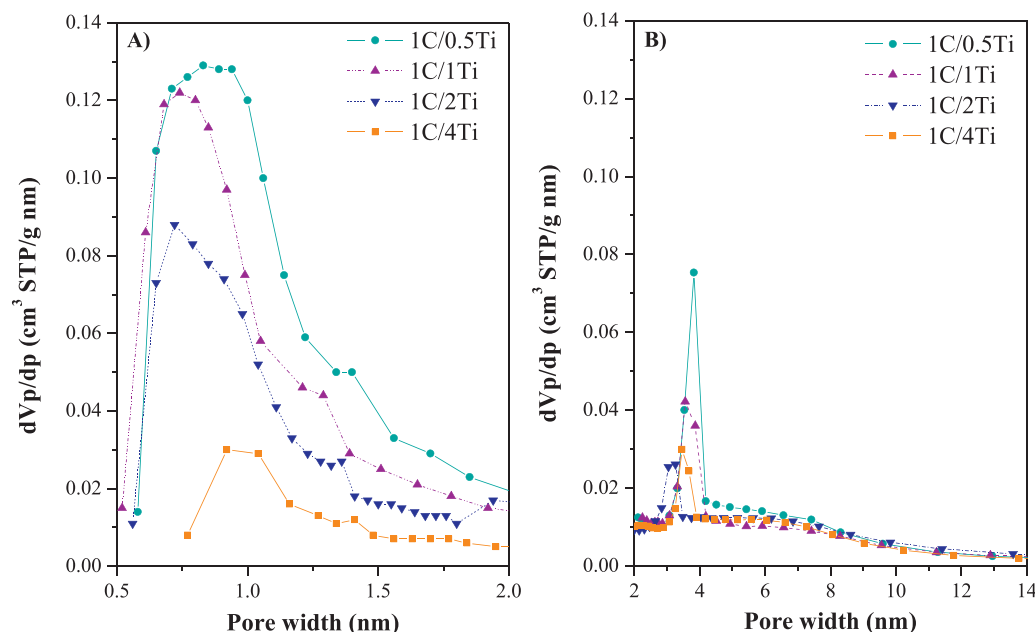
Fig. 6. Micropore (A) and mesopore (B) size distribution of the titania–clay heterostructures.

phase crystallized is the responsible of this light absorption in the UV region. Although sometimes the absorption edge can shift to the visible region due to the quantum size effect, in TiO$_2$ materials this effect is restricted to sizes below 10 nm due to their rather low exciton Bohr radii [41,42]. Therefore, the difference in the anatase crystal size has no effect on the electronic properties of the heterostructures synthesized. Band gap values have been estimated by assuming that TiO$_2$-based systems are indirect semiconductors [43] and using the Tauc Plot approximation [44]. This method allows determining the band edge by the equation $\alpha h\nu = A (h\nu – Eg)^{1/2}$ [45], where α, h, ν, Eg, and A represent the absorption coefficient, Planck constant, radiation frequency, band gap and a constant, respectively. From that equation, it is possible to build a plot of $(\alpha h\nu)^{1/2}$ vs. $h\nu$, called tauc plot (Fig. 7) [45], that shows a linear region just above the absorption edge whose extrapolation to the photon energy axis yields the semiconductor band gap value. The values calculated (included in Table 1) were similar for all the titania–clay heterostructures, analogous to those reported for anatase semiconductor [6,14]. Thus, the amount of TiO$_2$ assem-

bled to the clay does not show any apparent effect on the band edge of anatase.

3.2. Photocatalytic degradation of rhodamine B and phenol

The as-synthesized heterostructures were tested as photocatalysts for solar photodegradation of rhodamine B and phenol. It is well known that photocatalytic reaction occurs on the surface of the catalyst where the reactants are adsorbed. Therefore, previous adsorption tests were carried out considering the adsorption properties that characterize the clay materials [46]. Fig. S3 of ESI shows as example the adsorption of RhB and phenol in dark onto the 1C/2Ti catalyst under the conditions detailed in ESI. From the results of those tests an adsorption time of 2 h was established prior to each photocatalytic experiment. The adsorption tests showed that the titania–clay heterostructures have significantly more affinity for RhB than for phenol. This effect has been studied in detail in the literature for different clay materials and has been explained by the different types of interactions between dyes and clays, which include ion exchange of cationic dyes and dye interaction with the surface oxygen atoms of the clay [47]. Fig. 8 represents the
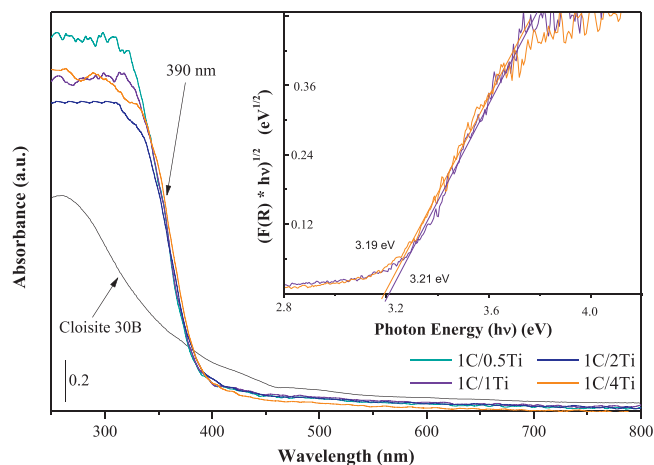

Fig. 7. DR-UV–vis spectra of the starting organoclay and the titania–clay heterostructures. Tauc plot of 1C/1Ti and 1C/4Ti heterostructures are plotted in the inserted figure.
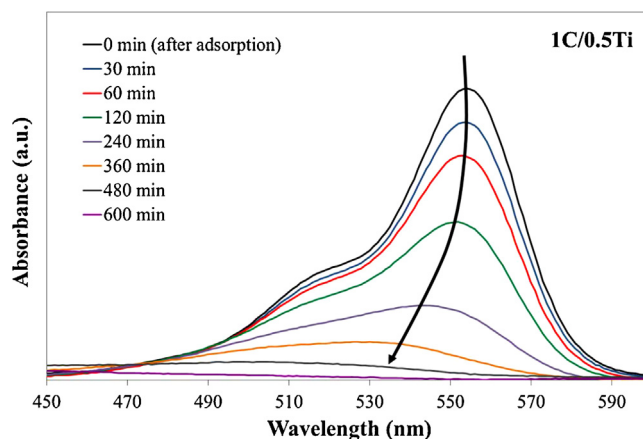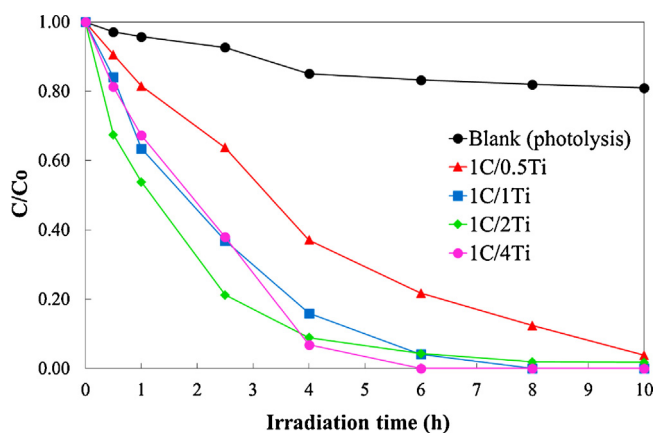

Fig. 8. UV–vis absorption changes of RhB in aqueous suspensions of 1C/0.5Ti as function of the irradiation time.
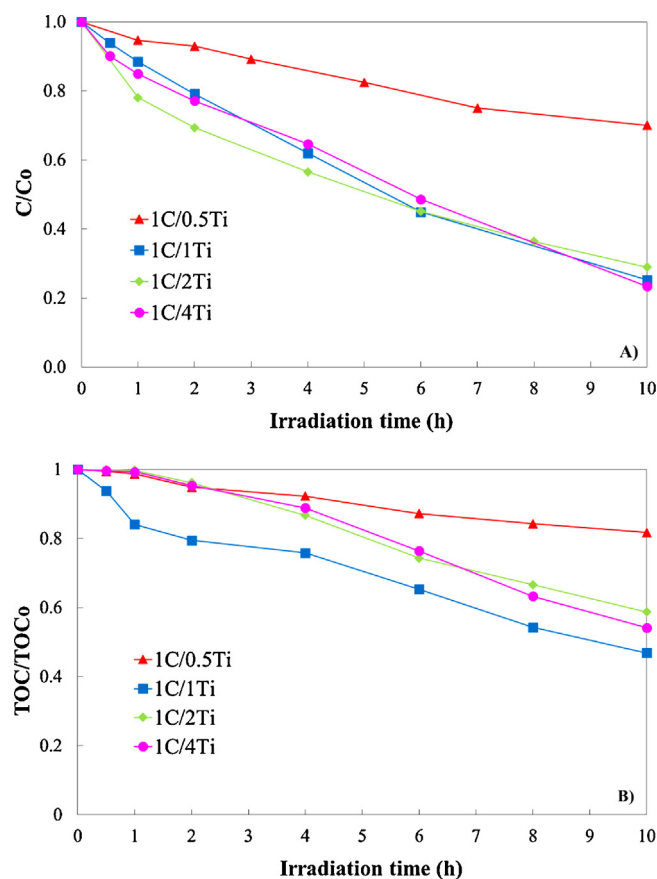
Fig. 9. Evolution of RhB concentration upon the irradiation time with the catalysts tested.

Fig. 10. Evolution of (A) phenol concentration and (B) TOC upon irradiation time with the catalysts tested.

evolutions of the spectral changes that occur upon RhB solar photodegradation with the 1C/0.5Ti catalyst. The trend was similar with the rest of the titania–clay heterostructures. In all cases, the characteristic absorption band of RhB decreased upon the irradiation time. It was also observed that solar irradiation provokes a shift of the maximum absorption toward lower wavelength values. This behavior has been previously described in the literature associated to the blue shift in the absorption band of the dye that is caused by the *N*-deethylation of the RhB, yielding to de-ethylated RhB byproducts showing maximum light absorption at 498 nm [48,49].
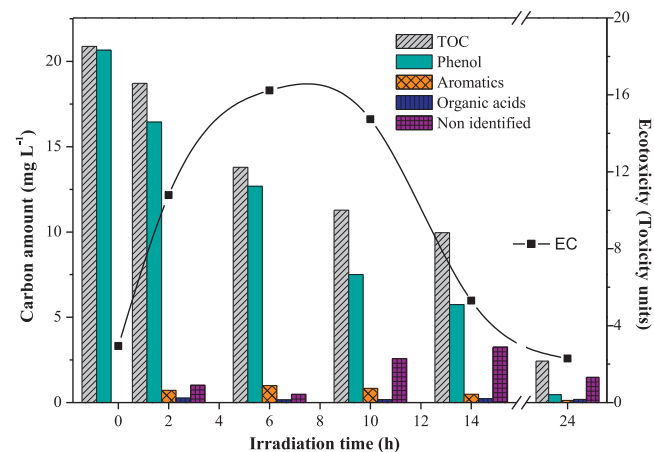
Fig. 9 shows the evolution of the RhB concentration upon the irradiation time with the catalysts tested. C_0 represents the initial concentration once the adsorption equilibrium was reached (after 2 h in dark). The titania–clay heterostructures synthesized appear fairly active for the degradation of RhB under solar light irradiation, as can be seen from the much higher RhB conversion reached in presence of these catalysts compared to that of the blank experiment. Complete conversion was achieved with the four catalysts although at different reaction rates depending on the titania/clay ratio. This activity is due to the TiO$_2$ formed in these heterostructures. It is known that titania particles induce the conventional photocatalytic mechanism characterized by the generation of OH$^\bullet$ and O$_2^{\bullet-}$ radicals [1,11] able to oxidize organic compounds, in our case induced by solar light. There seems to be an optimum relative amount of TiO$_2$ at a titania/clay ratio around 2. As discussed before the electronic properties and band gap values of the catalysts prepared were quite similar so that the differences found on their activities cannot be explained on the basis of those properties. Increasing the amount of TiO$_2$ means a higher concentration of the catalytic active phase but also a decrease of the surface area affecting not only to the total or BET surface area but also to the external or non-microporous area, namely the most accessible. Despite the complete conversion of RhB achieved, the TOC reduction (not shown) was almost negligible with all the catalysts tested. Thus, mineralization is not reached and some intermediates, not detected by UV–vis spectroscopy, are produced. This supports the *N*-dethylation mechanism described before for the degradation of RhB.

The catalysts were also tested for the solar photodegradation of phenol. As in the case of RhB, phenol adsorption was evaluated prior to the photocatalytic tests and very low adsorption, below 5%, was found (Fig. S3 of ESI). On the other hand, degradation of phenol was negligible after 10 h in the absence of catalyst. According to the results of Fig. 10, the catalysts tested show only a remarkable activity for phenol photodegradation, although significantly lower than that of RhB, due to the higher reactivity of the former. Under the experimental conditions phenol disappearance reached around
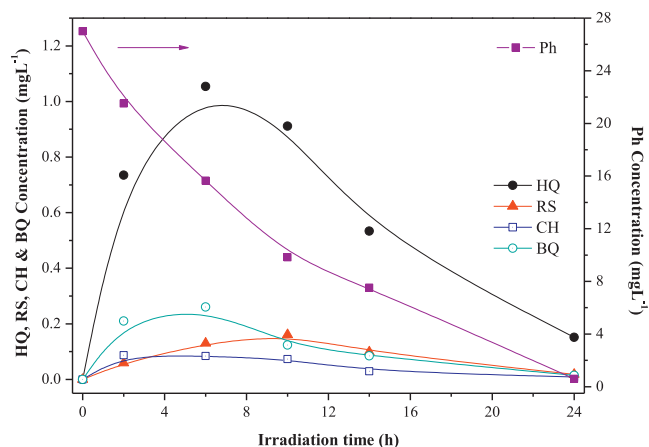
80% after 10 h of irradiation using the catalysts with higher amount of TiO$_2$ (1C/1Ti, 1C/2Ti and 1C/4Ti). However, in the case of phenol mineralization is now frankly higher than that observed for RhB, reaching close to 50% after 10 h with the 1C/1Ti catalyst. In order to check if higher mineralization degree could be obtained, an experiment was extended up to 24 h of irradiation time with the 1C/2Ti photocatalyst. Fig. 11 represents the evolution of TOC, phenol, aromatics, organic acids and other non-identified products, all in terms of carbon. The non-identified products have been estimated from the difference among the TOC measured and the TOC calculated

Fig. 11. Evolution of the TOC and the carbon amount measured from phenol, aromatic compounds, organic acids and non-identified byproducts upon irradiation time with the 1C/2Ti catalyst.

Fig. 12. Evolution of phenol (Ph), hydroquinone (HQ), resorcinol (RS), catechol (CH) and p-benzoquinone (BQ) upon irradiation time with the 1C/2Ti catalyst.

Table 2
Pseudo-first order rate constants (k) of RhB and phenol disappearance.

Catalyst	k RhB min^{-1}	k Phenol min^{-1}
1C/0.5Ti	0.0044	0.0006
1C/1Ti	0.0075	0.0022
1C/2Ti	0.0101	0.0022
1C/4Ti	0.0064	0.0023

from phenol and the identified reaction products (see Fig. S4 of ESI). As can be seen upon irradiation times of 24 h the mineralization reaches around 90% with almost complete disappearance of phenol and aromatic byproducts. This proves the significant activity of the catalyst.

Different works have proposed a photocatalytic degradation mechanism of phenol (under both UV and visible lights) through the formation of aromatic intermediates, mainly hydroquinone and benzoquinone, which afterwards are oxidized to different short-chain organic acids [50,51] (evolution of short-chain organic acids is represented in Fig. S5 of ESI). Finally, most of the intermediates produced are completely oxidized to CO_2 and H_2O as confirmed by the high mineralization achieved [52]. However, acetic and formic acids seem to be more refractory to photodegradation, which comprise a residual TOC fraction. While those species have no relevance in terms of ecotoxicity some of the intermediates detected in the degradation pathway of phenol are highly toxic species, most in particular hydroquinone and p-benzoquinone [53]. Then, it is very important to follow the evolution of those compounds. Fig. 12 shows the time course of the aromatic byproducts identified from phenol photodegradation with the 1C/2Ti catalyst. Hydroquinone (HQ), resorcinol (RS), catechol (CH) and p-benzoquinone (BQ) were detected by HPLC chromatography, always in very low concentrations, below 1 mg L^{-1} for HQ and much lower for the other compounds. Those aromatic intermediates showed maxima at different irradiation times and then their concentration decreased due to the photocatalytic degradation. In the case of the hydroquinone, the aromatic byproduct obtained at highest concentration and that of the highest toxicity [53], the concentration increased up to 7 h of irradiation time, and then decreased along the photocatalytic experiment. The presence of this aromatic compound, even at very low concentration can lead to fairly high values of ecotoxicity, well above those of the original phenol solution. Therefore, almost complete disappearance is required. Since the exhaustion of phenol and aromatics is needed to allow a substantial reduction of the ecotoxicity, it would be necessary to operate at long irradiation times, according to the results obtained. The evolution of ecotoxicity upon reaction time is also included in Fig. 11. That evolution is consistent with the time-course of the aromatic intermediates, most in particular hydroquinone, shown in Fig. 12. About 24 h of solar irradiation is needed to reduce the ecotoxicity below that of the starting phenol solution.

The degradation of the two target compounds tested (Figs. 9 and 10) is well described by a pseudo-first order rate equation, as can be seen from the plots of $\ln(C/Co)$ vs. irradiation time given in Fig. S6 of ESI. The pseudo-first order reaction rate

constants, k, estimated for photocatalytic degradation of both pollutants (RhB and phenol) with the different photocatalysts are summarized in Table 2. As can be seen, the values are significantly higher for RhB, confirming its higher reactivity. It is also clearly observed an increase of the k values with increasing the TiO$_2$ proportion up to a TiO$_2$/clay ratio of 2. Higher ratios result in a very similar k value for the photodegradation of phenol and a clear decrease for the photocatalytic decomposition of RhB. To learn more on the photocatalytic activity of these heterostructures, the photonic efficiency (ξ) was estimated from the reaction rate values [11]. We followed the Serpone methodology [54] considering the incident light intensity and using the photon flux calculated for our solar reactor, 9.76×10^{-5} einsteins s^{-1}. The ξ values for RhB photodegradation were 0.75, 1.28, 1.72 and 1.09 einstein s^{-1} with 1C/0.5Ti, 1C/1Ti, 1C/2Ti and 1C/4Ti, respectively, while decreased to 0.1, 0.38, 0.38 and 0.39 einstein s^{-1} for phenol photodegradation. These photonic efficiency values corroborate the higher reactivity of RhB that allows distinguishing more clearly between the four catalysts tested. Looking at the structural, electronic and textural properties of theses catalysts, 1C/4Ti has the highest TiO$_2$ amount but the lowest surface area and higher TiO$_2$ crystal size (Table S1 of ESI). These two features can be responsible of the detrimental effect on the k and ξ values for RhB photodegradation. Thus, while apparently higher TiO$_2$ amounts should improve the photocatalytic efficiency of the titania–clay heterostructures, the results reveal the existence of an optimum TiO$_2$ amount with regard to the catalytic activity.

4. Conclusions

We have applied a novel route based on a sol–gel approach for layered clay modification by incorporating nanostructured anatase particles. Several titania–clay photocatalysts were successfully prepared controlling the hydrolysis of the TiO$_2$ precursor while the exfoliation of the layered clay occurs. Thus, TiO$_2$ particles are assembled over the disordered clay layers yielding to photocatalysts with high surface area and a well-developed mesoporosity. By this way, only anatase was crystallized with small crystal sizes around 9–15 nm. The solar photocatalytic activity of theses titania–clay heterostructures is related to both the nanostructured titania particles and the textural properties. The synergistic effect between the surface of the clay and the photocatalytic activity of TiO$_2$, controlled by the amount and size of the anatase particles, determines the activity of these titania–clay heterostructures. Increasing the relative amount of TiO$_2$ means higher concentration of photocatalytic active phase but also decreases the available surface area. Thus, there is an optimum value of the titania/clay ratio, which according to the results so far seems to be somewhere within the 1–2 range. The photocatalysts prepared show promising activities in the degradation of RhB and phenol in water using solar light. In the case of phenol photodegradation, with irradiation times of 24 h the mineralization reaches very high values with an almost complete degradation of phenol and aromatic compounds and a decrease in the value of the initial ecotoxicity.

Acknowledgements

Appendix A. Supplementary data

Supplementary data associated with this article can be found, in the online version, at http://dx.doi.org/10.1016/j.apcatb.2015.04.004.

References

[1] M.N. Chong, B. Jin, C.W.K. Chow, C. Saint, Water Res. 44 (2010) 2997–3027.
[2] A. Fujishima, T.N. Rao, D.A. Tryk, J. Photochem. Photobiol. C 1 (2000) 1–21.
[3] S. Malato, P. Fernández-Ibañez, M.I. Maldonado, J. Blanco, W. Gernjak, Catal. Today 147 (2009) 1–59.
[4] M.D. Hernández-Alonso, F. Fresno, S. Suárez, J.M. Coronado, Energy Environ. Sci. 2 (2009) 1231–1257.
[5] H. Wang, L. Zhang, Z. Chen, J. Hu, S. Li, Z. Wang, J. Liu, X. Wang, Chem. Soc. Rev. 43 (2014) 5234–5244.
[6] M.R. Hoffman, S.T. Martin, W. Choi, D.W. Bahneman, Chem. Rev. 95 (1995) 69–96.
[7] O. Carp, C.L. Huisman, A. Reller, Prog. Solid State Chem. 32 (2004) 33–177.
[8] M. Anpo, M. Takeuchi, J. Catal. 216 (2003) 505–516.
[9] A. Fujishima, X. Zhang, D.A. Tryk, Surf. Sci. Rep. 63 (2008) 515–582;
K. Nakata, C. Terashima, A. Fujishima, Chem. Lett. 43 (2014) 1511–1513.
[10] J. Kiwi, C. Pulgarin, Catal. Today 151 (2010) 2–7.
[11] M. Pelaez, N.T. Nolan, S.C. Pillai, M.K. Seery, P. Falaras, A.G. Kontos, P.S.M. Dunlop, J.W.J. Hamilton, J.A. Byrne, K. O'shea, M.H. Entezari, D.D. Dionysio, Appl. Catal. B-Environ. 125 (2012) 331–349.
[12] M. Fernández-García, X. Wang, C. Belver, J.C. Hanson, J.A. Rodriguez, J. Phys. Chem. C 111 (2007) 674–682.
[13] H. Zhang, G. Chen, D.W. Bahnemann, J. Mater. Chem. 19 (2009) 5089–5121.
[14] S. Banerjee, S.C. Pillai, P. Falaras, K.E. O'shea, J.A. Byrne, D.D. Dionysiou, J. Phys. Chem. Lett. 5 (2014) 2543–2554.
[15] J.-M. Herrmann, J. Matos, J. Disdier, C. Guillard, J. Laine, S. Malato, J. Blanco, Catal. Today 54 (1999) 255–265;
J. Matos, J. Laine, J.-M. Herrmann, J. Catal. 200 (2001) 10–20.
[16] T. Cordero, J.-M. Chovelon, C. Duchamp, C. Ferronato, J. Matos, Appl. Catal. B-Environ. 73 (2007) 227–235.
[17] J. Liu, G. Zhang, Phys. Chem. Chem. Phys. 16 (2014) 8178–8192.
[18] D. Papoulis, S. Komarneni, D. Panagiotaras, E. Stathatos, D. Toli, K.C. Christoforidis, M. Fernández-García, H. Li, S. Yin, T. Sato, H. Katsuki, Appl. Catal. B: Environ. 132–133 (2013) 416–422.
[19] A. Corma, H. Garcia, Chem. Commun. 13 (2004) 1443–1459.
[20] S. Perathoner, G. Centi, Pillared Clays and Related Catalysts, in: A. Gil, S.A. Korili, R. Trujillano, M.A. Vicente (Eds.), Springer, New York, 2010.
[21] Z. Ding, H.Y. Zhu, G.Q. Lu, P.F. Greenfield, J. Colloid Interf. Sci. 209 (1999) 193–199.
[22] L. Chmielarz, B. Gil, P. Kustrowski, Z. Piwowarska, B. Dudek, M. Michalik, J. Solid State Chem. 182 (2009) 1094–1104.
[23] P. Aranda, C. Belver, E. Ruiz-Hitzky, Materials and clay minerals, in: L.F. Drummy, M. Ogawa, P. Aranda (Eds.), CMS Workshop Series, vol. 18, The Clay Minerals Society, 2013.
[24] Y. Zhang, D. Wang, G. Zhang, Chem. Eng. J. 173 (2011) 1–10.
[25] P. Aranda, R. Kun, M.A. Martín-Luengo, S. Letaief, I. Dékány, E. Ruiz-Hitzky, Chem. Mater. 20 (2008) 84–91.
[26] C. Belver, P. Aranda, M.A. Martín-Luengo, E. Ruiz-Hitzky, Microp. Mesop. Mater. 147 (2012) 157–166.
[27] S. Letaïef, E. Ruiz-Hitzky, Chem. Commun. (2003) 2996–2997.
[28] S. Letaïef, M.A. Martín-Luengo, P. Aranda, E. Ruiz-Hitzky, Adv. Funct. Mater. 16 (2006) 401–409.
[29] E. Manova, P. Aranda, M.A. Martín-Luengo, S. Letaïef, E. Ruiz-Hitzky, Microp. Mesop. Mater. 131 (2010) 252–260.
[30] Joint Committee on Powder Diffraction Standards, International Centre for Diffraction Data (ICDD).
[31] R.L. Snyder, J. Fiala, H.J. Bunge, Defect and Microstructure Analysis by Diffraction, Oxford University Press, New York, 1999.
[32] S. Brunauer, P.H. Emmett, E. Teller, J. Am. Chem. Soc. 60 (1938) 309–319.
[33] B.C. Lippens, J.H. De Boer, J. Catal. 4 (1965) 319–323.
[34] G. Horvath, K. Kawazoe, J. Chem. Eng. Jpn. 16 (1983) 470–475.
[35] G.P. Barrett, L.G. Joyner, R.H. Halenda, J. Am. Chem. Soc. 73 (1951) 373–380.
[36] E. Ruiz-Hitzky, P. Aranda, C. Belver, Manipulation on nanoscale materials: an introduction to nanoarchitectonics, in: K. Ariga (Ed.), The Royal Society of Chemistry, Cambridge, 2012, pp. 87–111.
[37] J. Rouquerol, F. Rouquerol, P. Llewellyn, G. Maurin, K.S.W. Sing, Adsorption by powders and porous solids, in: Principles Methodology and Applications, Academic Press, Oxford, 2013.
[38] T.J. Pinnavaia, M.-S. Tzou, S.D. Landau, R.H. Raythatha, J. Mol. Catal. 27 (1984) 195–212.
[39] M. Dijkstra, J.-P. Hansen, P.A. Madden, Phys. Rev. 55 (1997) 3044–3053.
[40] A. Gil, S.A. Korili, M.A. Vicente, Catal. Rev. 50 (2008) 153–221.
[41] Synthesis, Properties and Applications of Solid Oxides, in: J.A. Rodríguez, M. Fernández-García (Eds.), John Wiley, New York, 2007.
[42] H.-J. Zhang, L.-S. Wang, J. Am. Chem. Soc. 129 (2007) 3022–3029.
[43] M. Fernández-García, A. Martínez-Arias, J.C. Hanson, J.A. Rodríguez, Chem. Rev. 104 (2004) 4063–4104.
[44] J. Tauc, Mater. Res. Bull. 5 (1970) 721–726.
[45] M.A. Butler, J. Appl. Phys. 48 (1977) 1914–1920.
[46] G.J. Churchman, W.P. Gates, B.K.G. Theng, G. Yuan, Handbook of Clay Science, in: F. Bergaya, B.K.G. Theng, G. Lagaly (Eds.), Elsevier, 2006.
[47] R.A. Schoonheydt, C.T. Johnston, Handbook of Clay Science, in: F. Bergaya, B.K.G. Theng, G. Lagaly (Eds.), Elsevier, 2006.
[48] P. Qu, J. Zhao, T. Shen, H. Hidaka, J. Mol. Catal. A – Chem. 129 (1998) 257–268.
[49] C. Belver, C. Adan, M. Fernández-García, Catal. Today 143 (2009) 274–281.
[50] A. Turki, C. Guillard, F. Dappozze, Z. Ksibi, G. Berhault, H. Kochkar, Appl. Catal. B – Environ. 163 (2015) 404–415.
[51] J. Reszczyńska, T. Grzyb, J.W. Sobczak, W. Lisowski, M. Gazda, B. Ohtani, A. Zaleska, Appl. Catal. B – Environ. 163 (2015) 40–49.
[52] A.F. Mohedano, V.M. Monsalvo, J. Bedia, J. Lopez, J.J. Rodriguez, J. Environ. Chem. Eng. 2 (2014) 2359–2364.
[53] A. Santos, P. Yustos, S. Gomis, G. Ruiz, F. Garcia-Ochoa, Chem. Eng. Sci. 61 (2006) 2457–2467.
[54] N. Serpone, J. Photochem. Photobiol. A 104 (1997) 1–12.